Arabian Journal of Chemistry (2022) **15**, 103754

King Saud University

Arabian Journal of Chemistry

www.ksu.edu.sa
www.sciencedirect.com

ORIGINAL ARTICLE

Converting red mud wastes into mesoporous ZSM-5 decorated with TiO_2 as an eco-friendly and efficient adsorbent-photocatalyst for dyes removal

Riki Subagyo [a], Hellna Tehubijuluw [a,b], Wahyu Prasetyo Utomo [a,c], Hamdan Dwi Rizqi [a], Yuly Kusumawati [a,*], Hasliza Bahruji [d], Didik Prasetyoko [a]

[a] *Department of Chemistry, Faculty of Science and Data Analytics, Institut Teknologi Sepuluh Nopember, Kampus ITS Keputih, 60111, Sukolilo, Surabaya, Indonesia*
[b] *Department of Chemistry, Faculty of Mathematics and Natural Sciences, Pattimura University, Kampus Poka, 97134, Jl. Ir. M. Putuhena, Ambon, Indonesia*
[c] *School of Energy and Environment, City University of Hong Kong, Kowloon 999077, Hong Kong Special Administrative Region*
[d] *Centre of Advanced Material and Energy Science, Universiti Brunei Darussalam, Jalan Tungku Link, BE 1410, Brunei Darussalam*

Received 21 December 2021; accepted 30 January 2022
Available online 3 February 2022

KEYWORDS

ZSM-5;
TiO_2;
Dyes removal;
Photocatalytic

Abstract Red mud wastes have been converted into mesoporous zeolite socony mobile-5 (ZSM-5) followed by deposited titanium dioxide (TiO_2) nanoparticles to generate synergy adsorption-photodegradation for removal of dye removal in waste water. The amount of TiO_2 loading was varied to achieve optimum photocatalytic activity while maintaining the mesoporosity and high surface area of ZSM-5. Sol-gel method facilitated the formation of anatase TiO_2 on the ZSM-5. The fourier transform infrared spectra clarified the formation of Si–O–Ti at 957 cm^{-1} by the exchanging the hydrogen ion with titanium ion, which proved by decreasing the absorption band of Si–OH and Si–O interaction at 964 and 944 cm^{-1}, respectively. Sol-gel method also preserved the mesopore diameter of ZSM-5 at 3.5 nm which allow the diffusion of methylene blue (MB) molecules into the pores. However, the surface area and the pore volume were slightly reduced with increasing the TiO_2 loading. The adsorption performance of samples showed that the increasing in the TiO_2 loading led to the decreasing in the adsorption capacity. All samples showed the suitability towards the pseudo second order kinetic. The Langmuir isotherm was suitable to describe the adsorption mechanism by monolayer adsorption. Mesoporosity of ZSM-5 accelerated the adsorption of dye via the increase of mass transfer in the pore channel which confirmed by the low intercept of intra-particle diffusion model at the first stage. The photocatalytic test showed that 10% TiO_2 loading on

* Corresponding author.
E-mail address: y_kusumawati@chem.its.ac.id (Y. Kusumawati).
Peer review under responsibility of King Saud University.

Production and hosting by Elsevier

https://doi.org/10.1016/j.arabjc.2022.103754

the ZSM-5 exhibited the highest methylene blue removal followed by 5% and 20% TiO_2 loading. Optimization on the amount of photocatalyst and the pH of solution indicated the reaction favoured 1 g L^{-1} of catalysts and at alkaline pH. 10% TiO_2/ZSM-5 also exhibited high stability and reusability up to four reaction cycles. Photocatalytic performance of 10% TiO_2/ZSM-5 was further investigated on photodegradation of malachite green and rhodamine B organic dyes, which showed the photocatalytic efficiency of 73 and 88%, respectively. Superoxide radical, hydroxyl radical, and photogenerated electron were identified as the main active species for MB photodegradation based on the reduction of degradation rate following the addition scavenger molecules.

1. Introduction

Photocatalytic degradation is an efficient method for removal of organic pollutant in water (Guo et al., 2018; Ye et al., 2019; Zouzelka et al., 2016). Although various semiconductors have been designed to improve the efficiency of photodegradation reaction, titanium dioxide (TiO_2) is still the ideal choice of semiconductor mainly due to its high photocatalytic activity, non-toxic properties and commercial availability at relatively low price. Apart from that, TiO_2 has a strong oxidation potential, chemical and physical stability, with a relatively low negative impact when disposed to the environment (Han et al., 2020; Li et al., 2021; Mekprasart et al., 2021). Nevertheless, catalytic activity of TiO_2 as photodegradation catalysts can be further improved by introducing mesopore structure and increasing surface area, mainly to enhance the adsorption and diffusion of organic pollutants (Azami et al., 2021; Ma et al., 2018; Rahman et al., 2017). Table 1 summarised the activity of TiO_2 on several high surface area support for decomposition of organic pollutants. The studies suggested that the synergy between high surface area support such as carbon and aluminosilicate as adsorbent and photocatalytic activity of TiO_2 enhanced the removal efficiency via adsorption-photocatalytic steps.

Zeolite secony mobile-5 (ZSM-5) was investigated as adsorbent for dye removal from water (He et al., 2020; Liu et al., 2021; Pan et al., 2021). ZSM-5 is a chemically and mechanically stable material with surface hydrophobicity, ideal for adsorption of organic molecules (Brião et al., 2017; Shams-Ghahfarokhi and Nezamzadeh-Ejhieh, 2015; Tehubijuluw et al., 2021). Apart from that, the porosity of ZSM-5 can be altered via addition of second organic template or dealumination reaction, resulting a large pore opening for diffusion of bulky organic molecules (Hartati et al., 2020). In order to further enhance the performance of ZSM-5 for dye removal, incorporation with TiO_2 on ZSM-5 structure created a synergy between adsorption and photodegradation (Wellia et al., 2020). TiO_2 nanoparticles deposited within the mesopores will restrict particles growth of TiO_2 thus exposing larger surface area. In addition, high surface area of mesoporous ZSM-5 also increased the dispersion of TiO_2 in order to avoid particle agglomeration.

Derakhsan-Nejad have reported the immobilization of TiO_2 on the conventional ZSM-5 zeolite for removal of ethyl benzene vapour under UV irradiation (Derakhshan-Nejad et al., 2020). However, conventional ZSM-5 exhibit a small micropore size of 0.498 nm which led to poor adsorption performance for large molecules. The formation of mesoporous ZSM-5 can be done to overcome the limitation of diffusion rate and mass transfer which led to poor adsorption performance. Our group have synthesized mesoporous ZSM-5 from red mud (RM) wastes via hydrothermal method. RM is industrial waste from bauxite refinery contained valuable minerals such as silica (SiO_2), alumina (Al_2O_3), and iron oxide (Fe_2O_3). The minerals can be used as precursor for the synthesis of catalysts, directly used as adsorbent or for soil remediation (Wang and Liu, 2021; Wang et al., 2017; Weber et al., 2019; Yang et al., 2018). Conversion of RM waste from industries into valuable material is identified as sustainable approach to reduce waste accumulation. Safe storage of red mud (RM) also contributed to a high cost of operation in bauxite refining industry mainly due to its high alkalinity. Therefore utilization of RM as precursor for synthesis of advanced material provides alternative route to increase its value added properties (Gomes et al., 2016). The use of mineral from industrial waste is an interesting strategy to minimize the dependency on laboratory grade reagents that can contribute to high cost of production (Belviso et al., 2018; Cheng et al., 2021).

In this study, TiO_2/ZSM-5 composites were produced to generate synergy between adsorption and photodegradation for removal of methylene blue (MB) in waste water. The potential of RM as precursor for the synthesis of mesoporous ZSM-5 was investigated using a dual-hydrothermal method. Subsequently, TiO_2 was deposited on mesoporous ZSM-5 via sol–gel method at different weight loading. The effect of TiO_2 loading and the mesoporosity of ZSM-5 was investigated on the efficiency for MB removal via adsorption and photodegradation. MB is used as model dye pollutant which is widely used in medical, paper and textile industries (Frunza et al., 2018; Huang et al., 2019; Joseph et al., 2019; Svyatchenko et al., 2021). MB has a poor biodegradability and prevented the sunlight transmission and enervating photosynthesis process of the aquatic plant (Qin et al., 2016). In addition, MB showed a carcinogenic and mutagenic potential in human body (Tkaczyk et al., 2020). The pH and concentration of

Table 1 Summary of support material to enhance the photodegradation of TiO_2.

Support	Organic compound	Concentration (mg L^{-1})	Dosage (g L^{-1})	Contact time (h)	Light source	Efficiency (%)	Reference
Carbon aerogel	Dimethyl phthalate	2	0.1	3	Xe Lamp	90	(Cui et al., 2016)
Multi walled carbon nanotube	4-chlorophenol	12.9	–	5	UV lamp	70	(Zouzelka et al., 2016)
silica nanofibers	RhB	100	0.3	1.5	UV lamp	94.91	(Tang et al., 2018)
Activated carbon	Acetaminophen	5	0.25	3	Xe lamp	97	(Peñas-Garzón et al., 2020)
Activated carbon fibres	MB	10	–	1	Mercury lamp	98	(Shi et al., 2012)
Graphene	4-chlorophenol	12.9	–	5	UV lamp	98	(Kusumawati et al., 2017)
ZSM-5	Methylene orange	20	2	3	Max lamp	99	(Znad et al., 2018)
Montmorillonite	RhB	10	0.1	3	UV-C Lamp	87.5	(Dao et al., 2021)

MB solution, the amount of TiO_2/ZSM-5 photocatalyst, and the stability during photodegradation are investigated in order to obtain optimum condition for photocatalytic degradation of MB. TiO_2/ZSM-5 was further utilised for degradation of malachite green (MG) and rhodamine b (RhB). Finally, the reaction was carried in the presence of scavenger molecules to determine the mechanism of photodegradation.

2. Material and methods

2.1. Materials

The precursor, red mud waste was obtained from Bintan Island, Indonesia. All chemical, namely sodium hydroxide (NaOH, 99%), colloidal silica (Ludox, 30 wt% in water), tetrapropylammonium hydroxide (TPAOH, 40 wt% in water), cetyltrimethylammonium bromide (CTAB, ≥98%), titanium butoxide (Ti$(OBu)_4$, ≥97%), ethanol (C_2H_5OH, ≥99.8%), acetic acid (CH_3-COOH, ≥99%), methanol (MeOH, ≥99.8%), isopropanol (IPA, ≥99.5%), ascorbic acid (AA, ≥99%), potassium iodide (KI, ≥99%), dimethyl sulfoxide (DMSO, ≥99.9%), MB (≥82%), MG (≥90%), RhB (≥90%) was bought from Sigma–Aldrich.

2.2. Preparation of mesoporous ZSM-5 and TiO_2/ZSM-5

The preparation of ZSM-5 from RM was carried out based on our previous work (Tehubijuluw et al., 2021). High concentration of Fe_2O_3 in RM was removed in order to increase the concentration of Al_2O_3 and SiO_2. 10 g RM was mixed with 10 g NaOH and heated at 450 °C for two hours. The obtained solid was cooled followed by addition of 127.5 mL deionized water under constant stirring for 24 h. The filtrate was separated and dried at 105 °C for 24 h to obtain natrium alumina silicate in solid phase. The resulting solid (0.663 g) was dissolved in 24.67 mL deionised water and mixed with ludox (39.55 g) under constant stirring for eight hours. 20.34 g TPAOH solution was added to the solution followed by heating at 80 °C for nine hours in Teflon line autoclave. The mixture was cooled to room temperature and was added with 18.93 g CTAB under stirring for an hour. The mixture was reheated at 150 °C for 24 h. Due to the final pH of mixture was 13, the obtained solid was washed until the pH of supernatant was neutral (pH = 7) followed by drying for 16 h.

Preparation of TiO_2/ZSM-5 was carried using a sol gel method. Ti$(BuO)_4$ was mixed with C_2H_5OH (2 mL) and labelled as solution A. In addition, the solution B was prepared by mixing of 0.1 mL CH_3COOH, 0.4 mL H_2O and 4.25 mL C_2H_5OH. The solution B was added to the solution A and stirred for an hour. ZSM-5 was added to the mixture under constant stirring for an hour. The resulting mixture was aged for 24 h at room temperature and dried at 60 °C overnight. The solid was grounded and calcined for an hour in nitrogen (N_2) and six hours in air atmosphere at 550 °C. The quantity of TiO_2 was varied of 5, 10 and 20% (w/w) loading. The schematic of preparation of ZSM-5 and TiO_2/ZSM-5 was displayed in Fig. 1.

2.3. Characterization

The crystalline phase of the as-prepared sample was analysed using powder x-ray diffraction (XRD, PANanalytical X'pert Pro) with Cu Kα radiation in the range 2θ = 5–90°. Fourier transform infrared (FTIR, SHIMADZU 96500) spectrometer was employed to determine the functional group of photocatalyst via KBr method. Surface morphology and elemental distribution of photocatalyst was investigated by scanning electron microscope (SEM, JEOL 6360 LA) and transmission electron microscopy (TEM, Hitachi HT7700). The textural properties of the as-prepared samples were studied using a Nova 1200 e Quantachrome instrument in N_2 physisorption at 77 K. The degassing treatment was carried out at 573 K for three hours. In order to determine the optical absorption of the as-prepared samples, Ultraviolet–visible diffuse reflectance spectrophotometer (UV–Vis DRS, SHIMADZU UV-26001) was utilized followed by Kubelka-Munk analysis to calculate the band gap energy of the samples.

2.4. Adsorption performance of TiO_2/ZSM-5

To determine the adsorption–desorption equilibrium of MB, the as-synthesised mesoporous ZSM-5 was mixed with MB solution at different contact time of 15, 30, 60 and 90 min. The concentration of MB after adsorption was determined using UV–Visible spectrophotometer (thermo scientific Genesys10uv). The adsorption capacity was calculated by Eq. (1).

$$Q = \frac{(C_i - C_f)}{m} \times V \quad (1)$$

where Q is adsorption capacity (mg adsorbate/ g adsorbent), C_i and C_f are initial and final MB concentration (mg L^{-1}), V is MB volume (L) and m is mass of adsorbent (g). The adsorption capacity at equilibrium condition was determined by pseudo second order non-linear plot (Eq. (2)) as follow.

$$Q_t = \frac{k_2 Q_e^2 t}{1 + k_2 Q_e t} \quad (2)$$

where Q_t and Q_e were adsorption capacity at t and equilibrium (mg adsorbate/ g adsorbent), respectively. k_2 was rate constant of adsorption (g mg^{-1} min^{-1}) and t was time (min). The adsorption was repeated with TiO_2/ZSM-5 composites. The selection of pseudo second order in the depiction of adsorption kinetics was confirmed by a linear plot with a correlation coefficient value close to 1 as shown in Fig. S1.

2.5. Photocatalytic performance of TiO_2/ZSM-5

Photocatalytic activities of TiO_2/ZSM-5 at 5%, 10% and 20% weight loading for degradation of MB were determined using ultraviolet-light emitting diode (UV-LED) Lamp (EPILEDS, λ = 365 nm, P = 3 W m^{-1}) with cooling system. The design of the photocatalytic reactor was showed in Fig. 2. In order to achieve the adsorption–desorption equilibrium prior to photodegradation, the reaction mixture was kept in dark condition for 90 min before UV irradiation. Thermo scientific Genesys10uv was used to determine the absorbance of the solution after reaction by scanning at 664 nm. The effect of initial concentration, dosage, and pH was studied to investigate the optimization of photocatalytic reaction.

2.6. The effect of scavenger molecules

The effect of scavenger molecules was carried out to identify the reactive species responsible for MB degradation. MeOH,

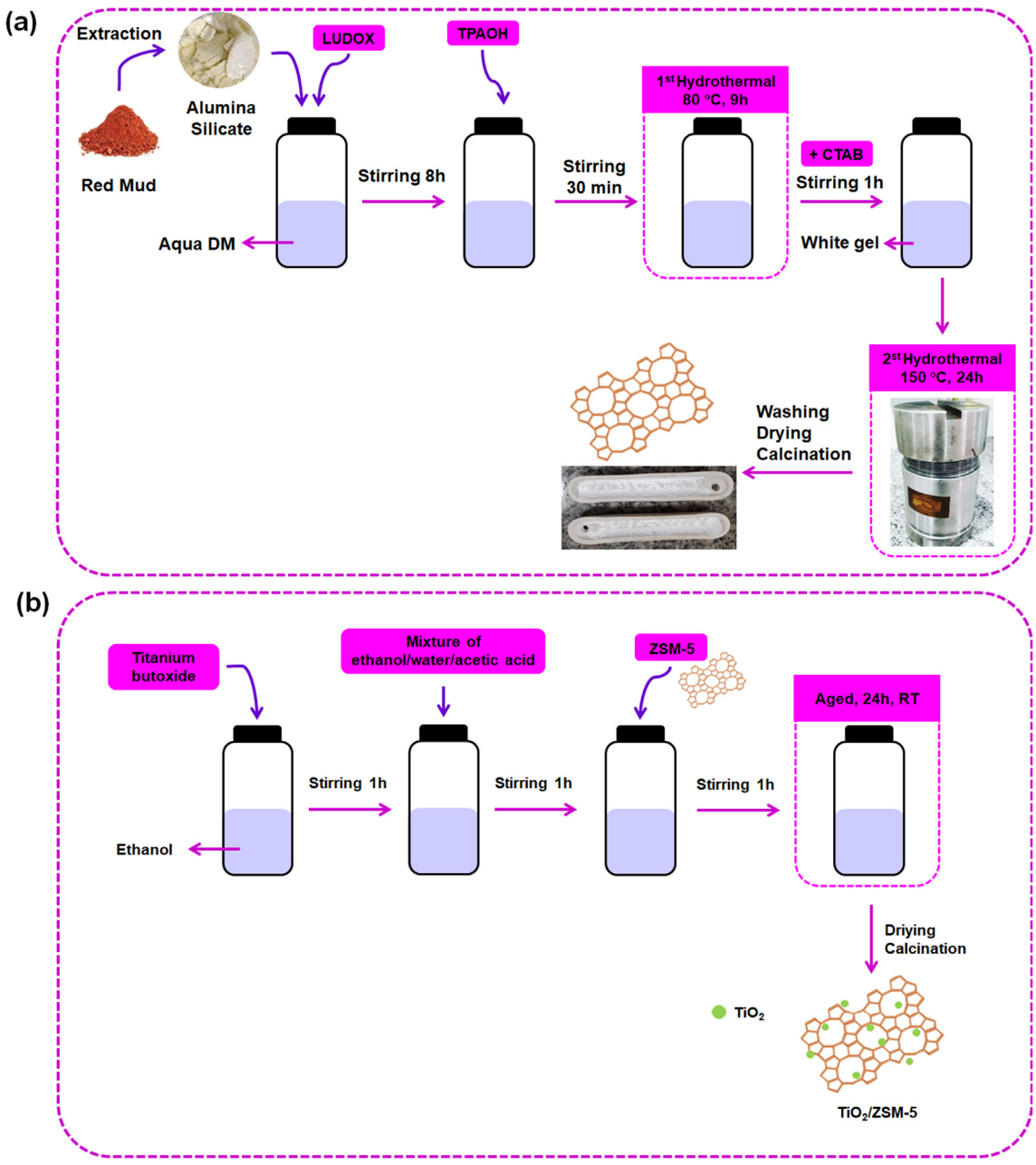

Fig. 1 The schematic of preparation of (a) ZSM-5 and (b) TiO_2/ZSM-5.

IPA, KI, DMSO and AA were considered as hole (h^+), hydroxyl radical in bulk ($\bullet OH_{bulk}$), hydroxyl radical in surface ($\bullet OH_{surf}$), electron and superoxide ion scavengers, respectively. 10% TiO_2/ZSM-5 was mixed with MB solution and scavenger solution (W = 1 g L^{-1}, C_{MB} = 100 mg L^{-1}) for three hours under UV-LEDs illumination.

3. Results and discussion

3.1. XRD analysis of samples

XRD analysis of mesoporous ZSM-5 and TiO_2/ZSM-5 photocatalysts were displayed in Fig. 3. Mesoporous ZSM-5 showed the characteristic peaks of ZSM-5 at 2θ = 7.9°, 8.8°, 23.18°, 23.96° and 24.47° corresponded to 101, 020, 501, 303 and 133 planes, respectively (Al-Jubouri, 2020). Impregnation with TiO_2 showed the formation of peaks at 2θ = 25.28°, 48.05°, 53.89°, and 55.06° corresponded to the respective 101, 200, 105, and 211 planes (JCPDS 21-1272). The peaks were characterised as anatase crystalline phase of TiO_2, with a significantly lower intensity compared to ZSM-5. The characteristic peaks of ZSM-5 were preserved following impregnation with a higher loading of TiO_2 indicating the stability of ZSM-5 framework. The intensity of anatase TiO_2 peaks were enhanced with increasing the amount of TiO_2 loading on ZSM-5.

3.2. FTIR analysis of samples

FTIR analysis was employed to characterise the functional group of mesoporous ZSM-5 and TiO_2/ZSM-5 composites as

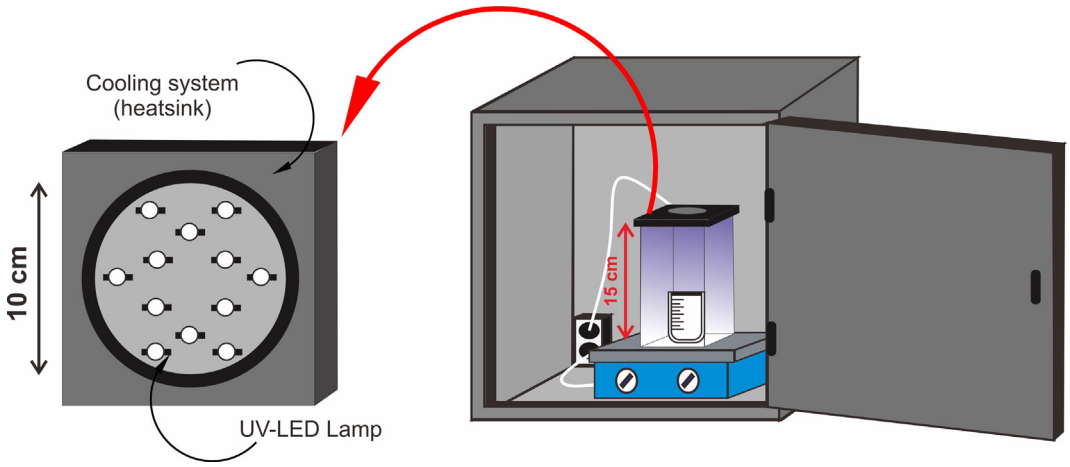

Fig. 2 Design of photocatalytic reactor with UV-LED lamp system.

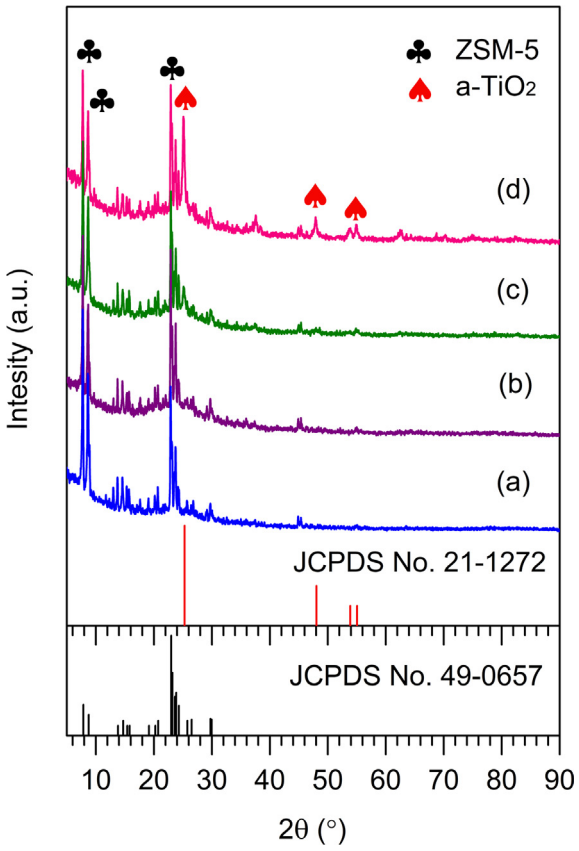

Fig. 3 XRD pattern of (a) ZSM-5, (b) 5% TiO_2/ZSM-5, (c) 10% TiO_2/ZSM-5, and (d) 20% TiO_2/ZSM-5.

shown in Fig. 4. The absorption band observed at 447 cm^{-1} in the as-prepared samples was assigned to the T–O–T (T is Al or Si atom) bending vibration of ZSM-5 (Tehubijuluw et al., 2021). D5R asymmetric stretching vibration was observed at 540 cm^{-1} which indicated the characteristic of MFI structure. The absorption peak at 798 and 1060 cm^{-1} corresponded to the external symmetric and internal symmetric stretching vibration modes of T–O–T, respectively. The asymmetric stretching mode was observed at 1220 cm^{-1}. The weak adsorption band at 1630 cm^{-1} attributed to the bending vibration of H–O–H bonds in water molecules adsorbed on zeolite. Increasing the TiO_2 loading on ZSM-5 showed the decreased on 540 cm^{-1} and 798 cm^{-1} bands intensity which suggested that increased number of titanium incorporated into the framework of ZSM-5. The absorption band at 930–970 cm^{-1} usually attributed to the Si–O–H bending vibration modes. However, those absorption was also ascribed to the Si–O–Ti vibration modes (Znad et al., 2018). In order to determine the absorption band of each functional groups, the evacuated of FTIR spectra in the range wavenumber of 1000–900 cm^{-1} was investigated as shown in Fig. S4. Si–O–H stretching band at 964 cm^{-1} decreased by the Ti addition into the ZSM-5, indicating that the ZSM-5 framework was rearranged during the sol–gel process, which was confirmed by the presence of new band at 957 cm^{-1}. This band clarified the formation of Si–O–Ti via sol–gel method by exchanging the hydrogen ion with titanium ion during the sol–gel process. Decreasing absorption band at 944 cm^{-1} which denoted as Si-O interaction proved the formation of Si–O–Ti. In addition, Si–O band also proved the Si and/or Al atom extraction from the main framework (Aziz et al., 2018). The spectra observation in the region of 500–400 cm^{-1} displayed the increasing the TiO_2 loading on ZSM-5 showed the decrease on 445 cm^{-1} band (T–O–T) followed by the increase on 423 cm^{-1} which was ascribed to Ti–O–Ti band.

3.3. Textural properties of samples

Textural properties of mesoporous ZSM-5 and after impregnation with TiO_2 were characterised using N_2 adsorption–desorption analysis as summarised in Table 2. Fig. 5 showed the type IV isotherm for the as-synthesised ZSM-5 based on IUPAC classification. Type IV isotherm indicated the typical adsorption–desorption characteristic of mesoporous material. The occurrence of hysteresis loop began at P/P_0 of 0.4 implied the capillary condensation in the ZSM-5 mesopores (Na et al., 2013). The increase of TiO_2 loading showed a gradual reduction of the specific surface area from 608.12 m^2 g^{-1} on mesoporous ZSM-5 to 503.43 m^2 g^{-1} at 20% of TiO_2 loading. At only 5% of TiO_2 loading, the surface area was only slightly reduced to 599.94 m^2 g^{-1} while the mesopore volume only

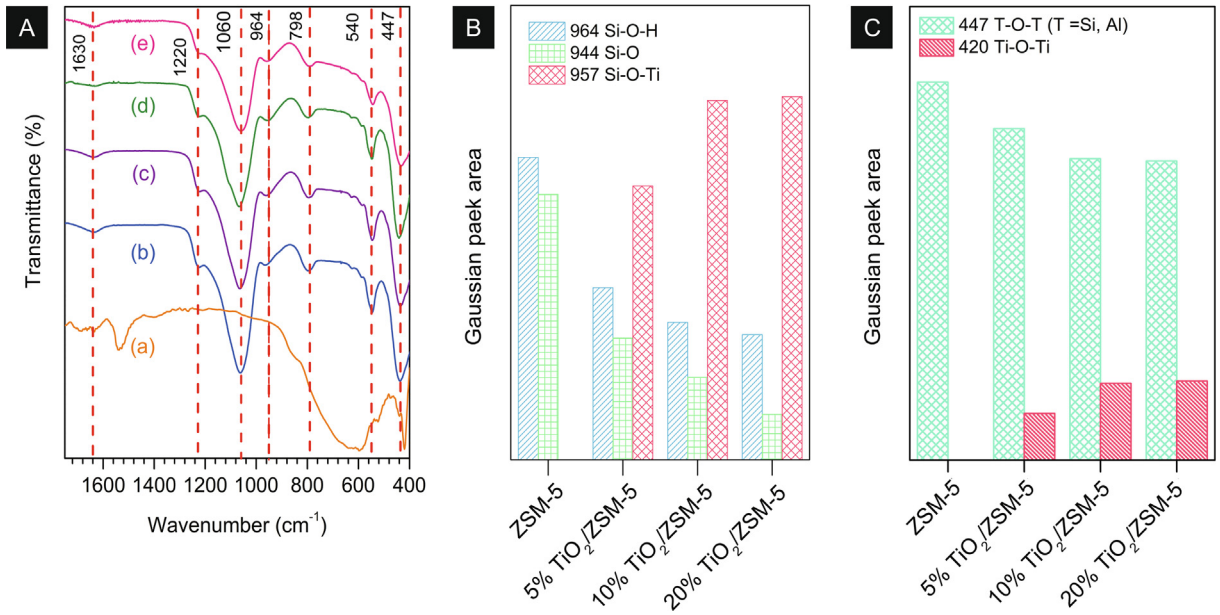

Fig. 4 (A) FTIR spectra of (a) ZSM-5, (b) 5% TiO_2/ZSM-5, (c) 10% TiO_2/ZSM-5, and (d) 20% TiO_2/ZSM-5; (B) Intensity of Gaussian peak area in the range 1000–900 cm^{-1} by evacuated system.

Table 2 Textural properties of the ZSM-5 and TiO_2/ZSM-5 composites.

Samples	S_{BET} (m^2 g^{-1})	Mesopore volume(cm^3 g^{-1})	Mesopore diameter(nm)	Bandgap(eV)
ZSM-5	608.12	0.577	0.304	–
5% TiO_2/ZSM-5	599.94	0.548	0.384	3.51
10% TiO_2/ZSM-5	527.46	0.455	0.307	3.30
20% TiO_2/ZSM-5	503.43	0.433	0.381	3.27

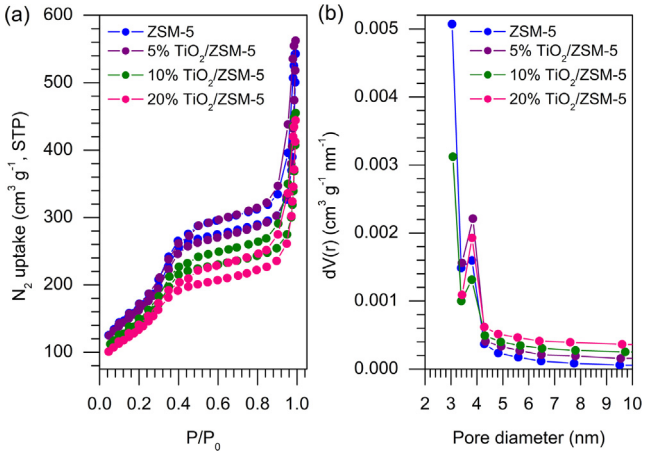

Fig. 5 N_2 adsorption–desorption (a) and (b) pore size distribution of the samples.

showed a slight reduction. There is a possibility that 5% TiO_2 formed nanoparticles within the mesopores without blocking the pores. Increasing the TiO_2 loading up to 10% significantly reduced the surface area and pore volume implying saturation of TiO_2 nanoparticles on the ZSM-5 external surface. The mesopore volume of ZSM-5 was reduced meanwhile no significant changes were observed on the size of pore diameter. Nevertheless, all TiO_2/ZSM-5 composites still preserved the Type IV isotherms which implied the preservation of ZSM-5 mesoporosity even after a higher loading of TiO_2.

3.4. Optical properties of samples

Fig. 6 showed UV–Visible spectra and Tauc's plot of ZSM-5 and TiO_2/ZSM-5 composites. The absorption in the UV area was enhanced following the addition of TiO_2 on ZSM-5. The presence of a higher loading of TiO_2 increased the adsorption of photon energy from UV light to generate charge carrier. The red shift in the absorption edge was observed with increasing the TiO_2 loading on ZSM-5, which attributed to the shift of band gap energy (Khan et al., 2014). Indirect transition of Tauc's plot was utilized to calculate the band gap energy of the as-prepared samples from the Eq. (3) (Makuła et al., 2018).

$$(\hat{I}\pm hv)^{1/2} = A(hv\text{-}E_g) \quad (3)$$

where hv is the photons energy, α is the coefficient of photon absorption, A is a proportional constant, and E_g is the band gap energy. According to Fig. 6b, the band gap energy of 5%, 10% and 20% TiO_2/ZSM-5 were determined at 3.51 eV, 3.30 eV, and 3.27 eV, respectively. A decrease in the TiO_2/ZSM-5 band gap energy with increasing of TiO_2 loading was

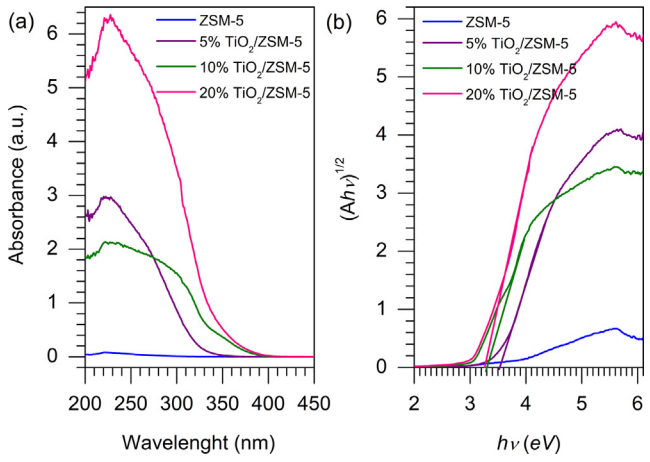

Fig. 6 UV–Visible spectra (a) and indirect Tauc's plot (b) of the as-prepared samples.

in a good agreement with the red shift of UV–visible light absorption.

3.5. Analysis of morphology

The morphology of mesoporous ZSM-5 and 10% TiO_2/ZSM-5 were characterised SEM and TEM to clarify the effect of TiO_2 on the ZSM-5. 10% TiO_2/ZSM-5 was chosen as a comparation due to the optimum of TiO_2 loading on the ZSM-5. Mesoporous ZSM-5 revealed the formation of micro-cubic crystallites structure which is the typical morphology of ZSM-5. Apart from that, non-uniformed aggregates with significantly smaller size was also formed presumably due to the presence of amorphous phase from incomplete crystallization process (Fig. 7a). The particle size distribution (PSD) histogram in Fig. 7c determined from the size of cubic crystallites revealed the average size of $\sim$ 2 µm. Following deposition with 10% TiO_2, no significant differences were observed on the morphology when compared to ZSM-5 (Fig. 7b). The results implied that TiO_2 was produced as nanoparticles that were not be able to distinguish using SEM analysis. The average crystal size of 10% TiO_2/ZSM-5 was slightly increased to $\sim$ 2.5 µm (Fig. 7d). The energy dispersive x-ray (EDX) spectra of 10% TiO_2/ZSM-5 in Fig. 7e showed the presence of aluminium (Al, 1.88 %w), silica (Si, 44.11 %w), oxygen (O, 51.05 %w) and titanium (Ti, 2.95 %w), which verified the successfully impregnation of TiO_2 on the ZSM-5. The distribution of the O atom marked the highest composition, confirming the configuration of tetrahedral SiO_4^{4-} and AlO_4^{5-} of ZSM-5. In addition, the highest composition of the O atom also indicated the configuration of TiO_2 which formed by calcination process.

TEM analysis was carried out to determine the morphology of ZSM-5 and after impregnation with 10% TiO_2. Fig. 8a showed mesoporosity of ZSM-5 was observed based on the formation of a clear density area within the ZSM-5 crystallite. Following impregnation with 10% TiO_2, the formation of TiO_2 particles on the surface of ZSM-5 was evidenced from the 0.35 nm lattice spacing ascribed to anatase (1 0 1) plane. TEM analysis determined that TiO_2 particles were mainly distributed on the external surface of ZSM-5. The particle size was estimated at $\sim$ 11–40 nm which confirmed by estimating crystallite size via XRD pattern in Table S4. TiO_2 particle agglomerate each other to form TiO_2 layer on the ZSM-5. It is interesting to observe that mesoporosity of ZSM-5 was retained, even after impregnation with TiO_2.

3.6. Adsorption of MB on TiO_2/ZSM-5

Fig. 9 showed the adsorption of MB on mesoporous ZSM-5 and TiO_2/ZSM-5 at different weight loading. The adsorption capacity was increased rapidly within 15 min of adsorption, followed with only a gradual increment up to 90 min as the adsorption reaching equilibrium. The rapid adsorption process was due to the presence of mesopores with the average diameter of $\sim$ 3.5 n m. Adsorbent with pore diameter between 2 and 5 nm allowed the diffusion of MB molecules within the pores, consequently increased the adsorption rate (Santoso et al., 2020). In addition, the adsorption onto external surface of the as-prepared samples also contributed to the increase of MB adsorption (Tehubijuluw et al., 2021). The adsorption of MB was plotted against the non-linear pseudo-second model which verified that ZSM-5 showed the highest adsorption capacity followed by 5% TiO_2/ZSM-5, 10% TiO_2/ZSM-5 and 20% TiO_2/ZSM-5. A large surface area of ZSM-5 provided a higher number of adsorption sites leading to the increase of adsorption. Following impregnation with TiO_2, the adsorption capacity was reduced particularly at higher TiO_2 loading, due to reduction of surface area and pore volume. The parameter of pseudo second order was displayed in Table S1 and Table S2. The parameter of pseudo first order was also calculated as a comparison. The pseudo second order model assumes that the process of adsorption was chemisorption (Tang et al., 2019). The experimental adsorption capacity at equilibrium was in agreement with the calculated pseudo second order adsorption capacity compare to the calculated pseudo first order adsorption capacity. With the increasing of the contact time, the rate of adsorption decrease, which is confirmed by the low of k_2 value. The intraparticle diffusion model was also used by Weber-Morris plot (Eq. (4)) to ensure if intraparticle diffusion is the rate-determining step of the adsorption process (Pathania et al., 2017).

$$Q_t = k_p t^{0.5} + C \tag{4}$$

k_p is the intraparticle diffusion rate constant (mg g^{-1} $min^{0.5}$) and C is a constant (mg g^{-1}). All samples consist two intersected segments (Fig. S2), confirms that adsorption goes through two stages: bulk diffusion and subsequent intraparticle diffusion. In the first stage, the MB molecules in the solution is transported through the particle interface. Due to the active site of adsorption, the rate of adsorption in the first stage is very fast, which is characterized by k_{p1} (Li et al., 2018). In the second stage, MB molecules diffuse into the pores of the particle, resulting in adsorption on the inner surface of each particle. At this stage, the diffusion resistance increases led to decrease in the rate of diffusion, which is confirmed by k_{p2}. The diffusion resistance was also confirmed by the intercept C that explained the boundary thickness information. The first stage intercept (C_1) was lower compare to the second stage intercept (C_2) indicated that the low external diffusion resistance. During the adsorption, the MB molecules were retained on the surface of particle. When the MB filled the adsorption sites, the free MB molecule mobility was obstructed which led to increase the diffusion resistance in the second stage (Bedin et al., 2016).

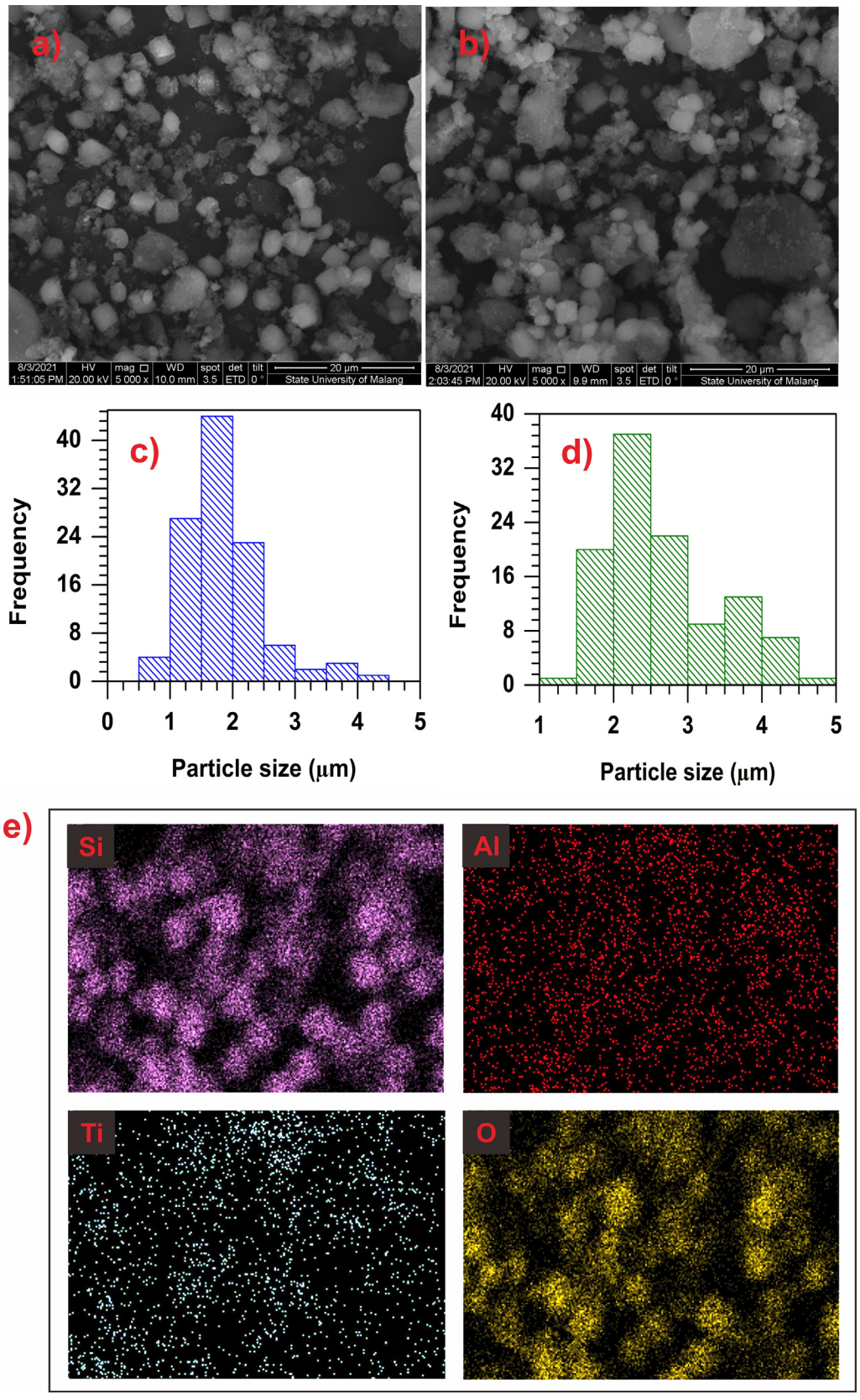

Fig. 7 Micrograph of ZSM-5 (a) and (b) 10% TiO_2/ZSM-5; PSD of (c) ZSM-5 and (d) 10% TiO_2/ZSM-5; (e) EDX images of 10% TiO_2/ZSM-5.

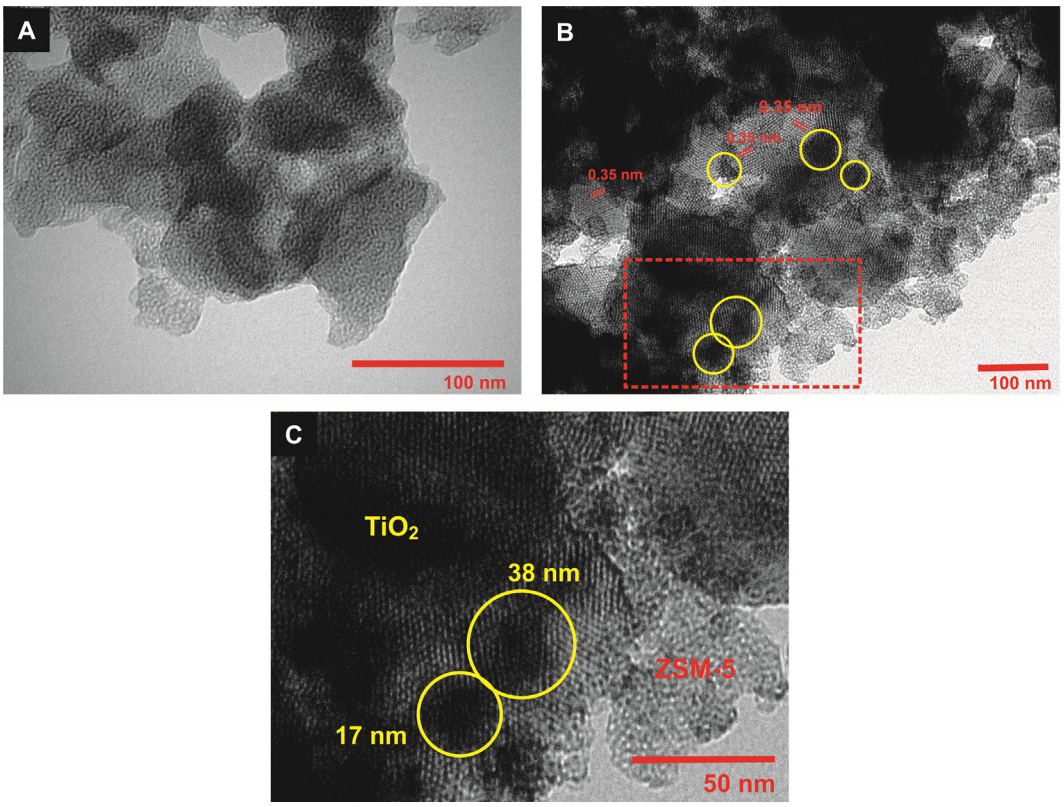

Fig. 8 TEM images of (a) mesoporous ZSM-5, (b) 10 %TiO_2/ZSM-5 and (c) inset of (b).

To provide the interaction mechanism of MB adsorption on the 10% TiO_2/ZSM-5, the adsorption isotherm was carried out using non-linear Langmuir, Freundlich and Temkin isotherm models as displayed in Eqs. (5), (6) and (7).

$$Q_e = \frac{Q_t K_L C_e}{1 + K_L C_e} \tag{5}$$

$$Q_e = K_F (C_e)^{1/n} \tag{6}$$

$$Q_e = B \ln K_T + B \ln C_e \tag{7}$$

Q_m, Q_e, and C_e were the maximum Langmuir adsorption capacity (mg g^{-1}), the adsorption capacity (mg g^{-1}) and the concentration (mg L^{-1}) of methylene blue ad equilibrium, respectively. K_L(L mg^{-1}), K_F (mg g^{-1})(L $mg^{-1})^{1/n}$ and K_T (L mg^{-1}) were the constant of Langmuir, Freundlich and Temkin. n and B ($\frac{RT}{b_T}$) were the dimensionless constant indicates to the adsorption intensity and the Temkin constant relations to the heat of adsorption, respectively.

According to Fig. S3, the MB adsorption on the 10% TiO_2/ZSM-5 followed Langmuir isotherm fitting. The result was supported by the lowest root mean square error (RMSE) value of Langmuir model compare to the RMSE value of Freundlich and Temkin model. The Langmuir model explained the monolayer MB adsorption on the 10% TiO_2/ZSM-5. The Langmuir isotherm characteristic was also evaluated using a equilibrium parameter (R_L), which following Eq. (8)

$$R_L = \frac{1}{1 + k_L C_0} \tag{8}$$

k_L is the Langmuir constant (L mg^{-1}) and C_0 is the initial dye concentration (mg L^{-1}). The R_L value (Table S2) was between 0 and 1, implied that the MB adsorption on the 10% TiO_2/ZSM-5 was a favorable process (Tehubijuluw et al., 2021).

3.7. Photocatalytic degradation of MB on TiO_2/ZSM-5

Photocatalytic degradation of MB on TiO_2/ZSM-5 composites were carried out to determine the optimum loading of TiO_2 for MB degradation. Photodegradation was carried out using 20 mL of 90 mg L^{-1} MB solution with 0.02 g of photocatalysts for three hours. Based on the adsorption result in Fig. 9, the photocatalysts suspension in MB solution was left in the dark for 90 min before illumination in order to ensure the adsorption–desorption have reached equilibrium. Fig. 10a showed the percentage of MB removal when using different loading of TiO_2 on ZSM-5. Note that, no photodegradation was observed when using mesoporous ZSM-5 as catalysts. However, the reduction of MB concentration at 55% in Fig. 10a was ascribed to the removal via adsorption. 5% and 10% TiO_2 on ZSM-5 exhibited more than 90% of MB degradation, which were significantly higher than 20% of TiO_2 loading. The presence of low loading TiO_2 at 5% was sufficient to catalyse photodegradation reaction. The importance of synergy between TiO_2 and ZSM-5 mesoporosity was evidenced by the decreased of photodegradation efficiency when at 20% of TiO_2 loading. Although at 20% of TiO_2 loading enhanced photon adsorption in UV region, the decrease in surface area

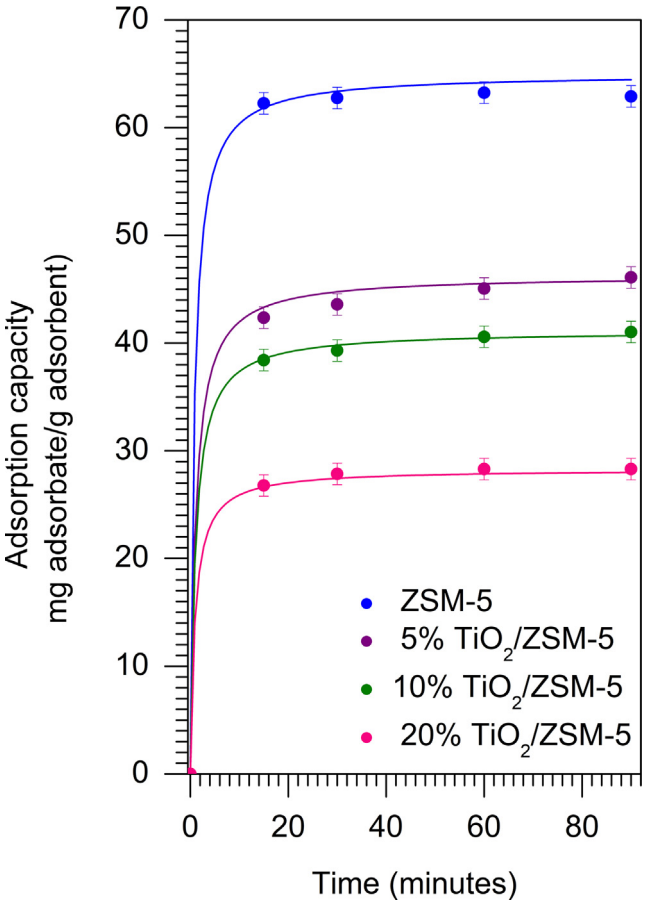

Fig. 9 Adsorption of methylene blue on the as-prepared samples (W = 1 g L^{-1}, C_{MB} = 90 mg L^{-1}, 33 ± 3 °C).

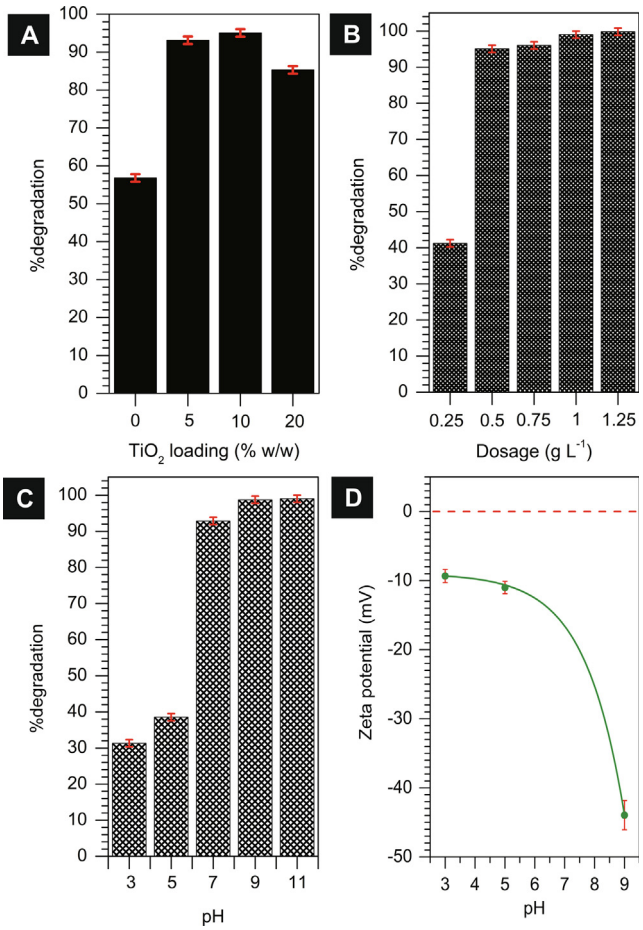

Fig. 10 Optimization studies on the effect of (a) TiO_2 loading on ZSM-5; (b) the amount of 10% TiO_2/ZSM-5 photocatalyst dosage in the solution; (c) the pH of solution towards the percentage of MB degradation (C_{MB} = 90 mg L^{-1}, t = 3 h, 33 ± 3 °C); (d) zeta potential of 10% TiO_2/ZSM-5.

and pore volume reduced the available sites that were crucial for MB adsorption.

Optimization studies on the photocatalytic degradation of MB provides information on the amount of catalysts required for efficient adsorption of photon, but at the same time prevented the agglomeration of catalyst in the suspension (Deshmukh et al., 2020). The effect of photocatalyst dosage was carried out at 0.25, 0.5, 0.75, 1, and 1.25 g L^{-1}. According to Fig. 10b, the photodegradation of MB was significantly enhanced when the amount of catalysts were increased from 0.25 g L^{-1} to 0.5 g L^{-1}. The degradation efficiency of MB substantially enhanced from 41 to 99% with increasing the dosage after three hours of irradiation time. At much higher catalysts dosage, the degradation has reached optimum value with no significant enhancement was observed. These results verified that increasing of photocatalyst concentration in the solution provide the necessary adsorption and photocatalytic sites. However, no significant increase in photodegradation efficiency was observed with further addition of photocatalyst in the solution up to 1.25 g L^{-1}.

The effect of pH on MB degradation was investigated by variation of pH in acid and alkaline regions (Fig. 10c). Increasing the pH above 9 showed negligible differences on photodegradation efficiency suggesting the stability of TiO_2/ZSM-5 photocatalysts in alkaline condition. However, at low pH i.e. acidic condition, the degradation was significantly reduced to only 30%. The results further confirmed the importance of synergy between adsorption on mesoporous ZSM-5 and TiO_2 in order to promote photodegradation of MB. According to zeta potential analysis, ZSM-5 was protonated upon receiving H^+ from acid leading to the increase of electrostatic repulsion with the cationic molecule of MB in acidic solution. The electrostatic repulsion prevented MB molecules to adsorb on ZSM-5 surfaces thus reducing the degradation efficiency. On the other hand, in alkaline condition (10)% TiO_2/ZSM-5 surface was saturated with negatively charge OH^-, facilitated the adsorption of MB molecules due to electrostatic attraction. In addition, high concentration of OH^- molecules increased the formation of hydroxyl radical responsible for dye oxidation (Ma et al., 2016; Park et al., 2018).

3.8. The kinetic of MB photodegradation

The kinetic of MB photodegradation was determined at different initial concentration of MB solution between 100 and 130 mg L^{-1}. Fig. 11a showed that the degradation of MB was reduced with increasing of MB concentration. Detail

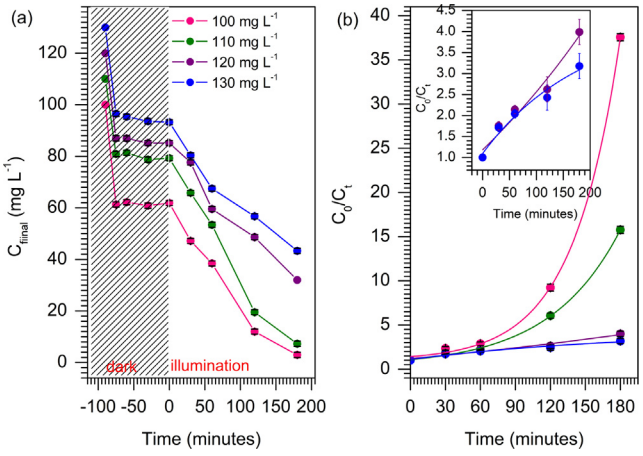

Fig. 11 The effect of concentration (a) and (b) the photokinetic of MB degradation by nonlinear plot of first order.

analysis on the amount of MB adsorbed on the TiO_2/ZSM-5 prior to light irradiation provides insight into the mechanistic route of the degradation. It is clear that, the increase of MB concentration reduced the amount of MB molecules that were physically adsorbed on TiO_2/ZSM-5. The adsorption reached equilibrium within the first 15 min of dark adsorption. No further removal of MB molecules from the solution when the adsorption was extended to 90 min. Note that, control experiment was also conducted in dark condition for 180 min (Fig. 12). The rapid adsorption was occurred at initial stage of adsorption process and reached equilibrium after 30 min. No obvious changes were observed when the reactions were carried out in the absence of UV light irradiation up to 180 min. The adsorption of MB on TiO_2/ZSM-5 strongly depended on the concentration of MB solution. At 100 mg L^{-1} of MB concentration, approximately 45% of MB was removed from the solution via adsorption, followed with photodegradation to achieve complete MB removal. Exposure to UV light continuously reduced the concentration of MB in the solution via photodegradation. A higher concentration of

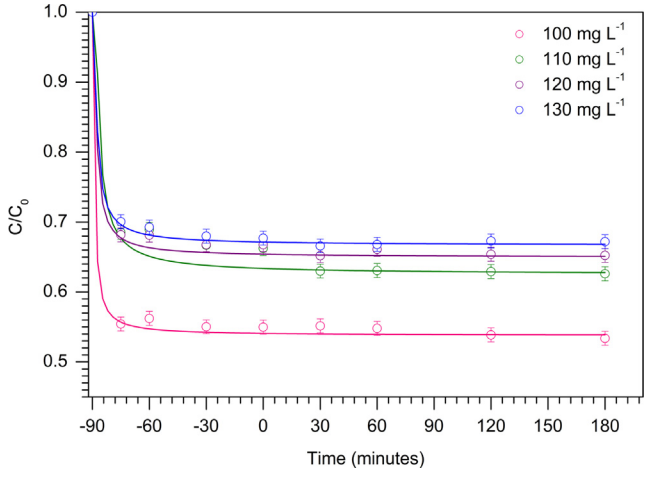

Fig. 12 MB photodegradation over 10% TiO_2/ZSM-5 at variation of MB concentration in dark condition (W = 1 g L^{-1}, t = 3 h, 30 ± 3 °C).

MB created an accumulation of MB molecules in the solution which consequently shielded the light from penetrating into 10% TiO_2/ZSM-5. MB is a photoactive molecule, which is able to absorb photon in UV and visible region. Saturation of MB in the solution may reduce the amounts of adsorbed photons for generation of electron and hole. Since the photocatalyst was already saturated with MB molecules, the generated energy carriers will be utilised to degrade the adsorbed molecules, before proceeding to oxidise MB in the solution. The low number of adsorbed photons led to reduction of hydroxyl radical formation consequently reduced the photocatalytic efficiency. The kinetic of MB photodegradation was determined according to the non-linear first order (Eq. (9)).

$$\frac{C_0}{C_t} = e^{k_{app}t} \tag{9}$$

where C_0 and C_t represent the MB concentration at initial and t = t, respectively. k_{app} represent the rate constant of first-order reaction. The nonlinear plot of C_0/C_t over irradiation time showed in Fig. 11b indicated that MB photodegradation by 10% TiO_2/ZSM-5 followed the first order kinetic model. The k_{app} was summarized in Table 3 revealed the k_{app} decreased by increasing of initial concentration. This indicated that the photodegradation was favourable at low concentration.

3.9. Stability and reusability of 10% TiO_2/ZSM-5

The stability of photocatalyst is another important parameter to determine its efficiency for large scale application. Therefore, the stability of 10% TiO_2/ZSM-5 was investigated up to four reaction cycles. The photocatalysts was filtered off the solution and calcined at 550 °C to remove any residual pollutants. Photocatalytic activity of 10% TiO_2/ZSM-5 showed ~ 99% of MB removal up to four cycles of reactions (Fig. 13a). Dark adsorption of MB on TiO_2/ZSM-5 also similar after four reaction cycles, removing up to 45% of MB via adsorption. The results indicated the stability of mesoporous ZSM-5 to retain its adsorption sites. When the saturated photocatalyst was exposed to UV light, the rate of photodegradation was slightly reduced from removing up to 90% of MB within 100 min to only 70% in 100 min after the four consecutive cycles. Nevertheless, the catalyst managed to achieve ~ 95% of MB removal when the light irradiation was extended up to 200 min. The photocatalyst retrieved after four reaction cycles was characterized using XRD. As shown in Fig. 13b, the XRD pattern of the spent photocatalyst (10% TiO_2/ZSM-5) showed no obvious changes on the diffraction angles and the intensity of the peaks that were ascribed to ZSM-5. However, the intensity of anatase peaks were slightly

Table 3 Photodegradation at different initial concentrations of MB and first-order constant values for MB degradation using 10% TiO_2/ZSM-5.

Initial conc.C_o (mg L^{-1})	Rate, k_{app} ($\times 10^{-3}$ min^{-1})	Initial rate, r_o ($\times 10^{-1}$ mg L^{-1} min^{-1})
100	17.1	17.10
110	13.6	14.96
120	5.2	6.24
130	4.1	5.33

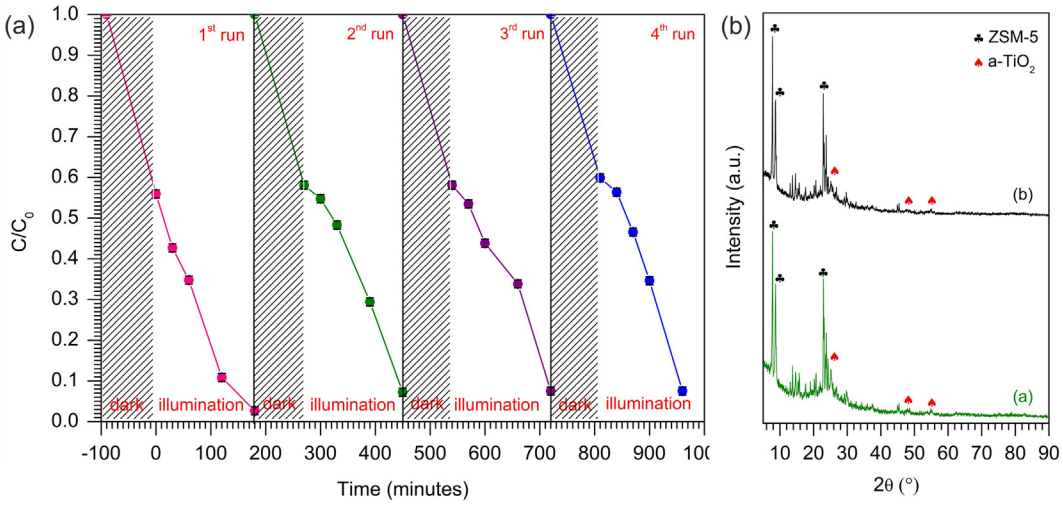

Fig. 13 (a) Reusability of 10% TiO_2/ZSM-5 in photodegradation of MB (C_{MB} = 100 mg L^{-1}, W = 1 g L^{-1}, t = 3 h, 33 ± 3 °C) and (b) XRD pattern of fresh and spent 10% TiO_2/ZSM-5.

reduced suggesting the changes of TiO_2 structural properties, which supported the slight reduction on MB degradation. The heat treatment to remove residual pollutant from 10% TiO_2/ZSM-5 led to the phase change from anatase phase to rutile phase. Evacuated system was used to investigate the anatase and rutile phase in the range of 25–28° as shown in Fig. S6. Fresh 10% TiO_2/ZSM-5 exhibited only anatase peak in the XRD pattern, while the spent 10% TiO_2/ZSM-5 exhibited anatase and rutile peak. The anatase peak of spent 10% TiO_2/ZSM-5 decrease compare to fresh 10% TiO_2/ZSM-5, which was followed by the presence of rutile phase. The slightly reduction on MB degradation by spent 10% TiO_2/ZSM-5 verified the presence of rutile phase was not suitable for UV induced photocatalytic. The result was also confirmed by Mustapha et al. which used rutile TiO_2 for MB photodegradation and exhibited the low efficiency (33%) under UV irradiation (Mustapha et al., 2017).

The potential of 10% TiO_2/ZSM-5 as photocatalyst was also investigated in the photodegradation of different types of dyes i.e. MG and RhB. The photocatalytic degradation of MG and RhB were carried out at similar reaction condition as photodegradation of MB. Malachite green and Rhodamine B are cationic dye as MB, which have the ability to adsorb strongly on negatively charged adsorbent. As shown in Fig. 14, 10% TiO_2/ZSM-5 catalysed photodegradation of RhB at approximately faster rate compared to photodegradation of MG. Dark adsorption prior to photodegradation also revealed a higher adsorption capacity at 58% of removal for MG compared to only 40% of RhB removal. However, upon exposure to UV irradiation, the degradation of RhB occurred faster to achieve 88% of RhB removal compared to MG at 73% of removal. Nevertheless, the results confirmed the ability of TiO_2/ZSM-5 as adsorbent and photocatalyst for removal of various type of organic dye pollutants in waste water.

3.10. Mechanism of photocatalytic degradation of MB

The synergy created between mesoporous ZSM-5 adsorbent and TiO_2 photocatalyst is beneficial to accelerate removal of

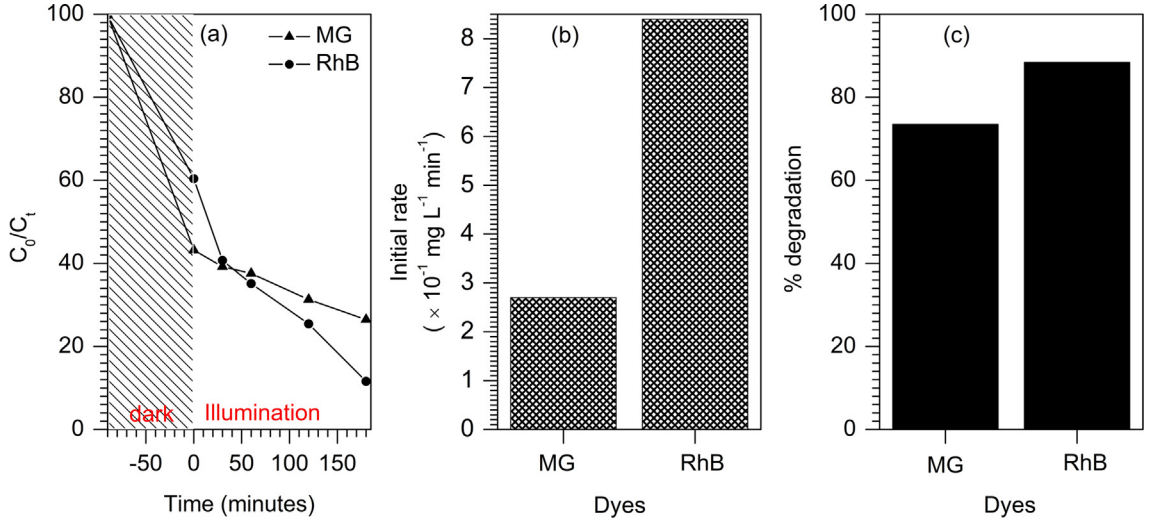

Fig. 14 Photocatalytic degradation of malachite green (MG) and Rhodamine B (RhB) on 10% TiO_2/ZSM-5.

MB and to improve the stability of photocatalysts. The mechanism of MB photodegradation over TiO_2/ZSM-5 composite was determined based on the charge transfer mechanism on TiO_2 and the effect of scavenger molecules. The valence band (VB) and the conduction band (CB) of 10% TiO_2/ZSM-5 at the zero charge was calculated based on the electronegativity concept using Butler and Ginley equation (Eqs. (10) and (11)) (Aziz et al., 2021a, 2021b) as follows:

$$E_{\mathrm{VB}} = X - E^{e} + \frac{1}{2}E_{g} \tag{10}$$

$$E_{\mathrm{CB}} = E_{\mathrm{VB}} - E_{\mathrm{g}} \tag{11}$$

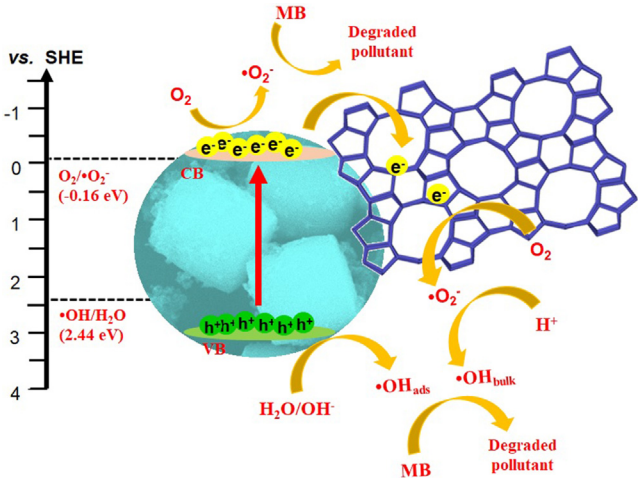

Fig. 15 Proposed mechanism of photodegradation of MB using 10% TiO_2/ZSM-5.

where E_{VB} and E_{CB} were the potential level of valence and conduction band, respectively, X is the absolute electronegative of the semiconductor which is for $TiO_2 \sim 5.81$ eV (Hafeez et al., 2019). E^e is the energy of free electron on hydrogen scale (4.5 eV) and E_g is the band gap energy of semiconductor. The calculated E_{VB} and E_{CB} of 10% TiO_2/ZSM-5 were determined at 2.96 and −0.34 eV, respectively.

When the UV light was irradiated onto 10% TiO_2/ZSM-5, the absorbed photon provided energy for electron excitation from CB to VB level. Meanwhile, similar number of holes were produced on the VB level. Since the CB potential was more negative than the $O_2/\bullet O_2^-$ potential (~−0.16 for SHE), the reduction of O_2 to $\bullet O_2^-$ by the excited electron was a feasible pathway for the photogenerated electron (Fauzi et al., 2022). The photogenerated electron travelled to the surface and reacted with oxygen gas generating superoxide radical $\bullet O_2^-$. The superoxide radical subsequently reacted with surface hydroxyl group to form $\bullet OH_{bulk}$ formation, or transferred into OH^- anion in the solution to form •OH radical. The generated $\bullet O_2^-$ and •OH reactive species oxidized MB molecule via multiple intermediates which ultimately produced CO_2 and H_2O. Apart from that, since the VB level is more positive than the $H_2O/\bullet OH$ potential (~2.44 eV for SHE), the photogenerated h^+ was also favourable to produce •OH. The suggested mechanism of MB photocatalytic degradation over 10% TiO_2/ZSM-5 was shown in Fig. 15.

In order to confirm the proposed mechanism, the effect of scavenger molecules on the activity of the catalysts were carried out to provide insight into the reactive oxygen species that was responsible for degradation of MB. Photodegradation of MB while using 10 %TiO_2/ZSM-5 was performed with the addition of several scavenging agents (Fig. 16). MeOH was added to the solution as h^+ scavenger (Lin et al., 2018) that

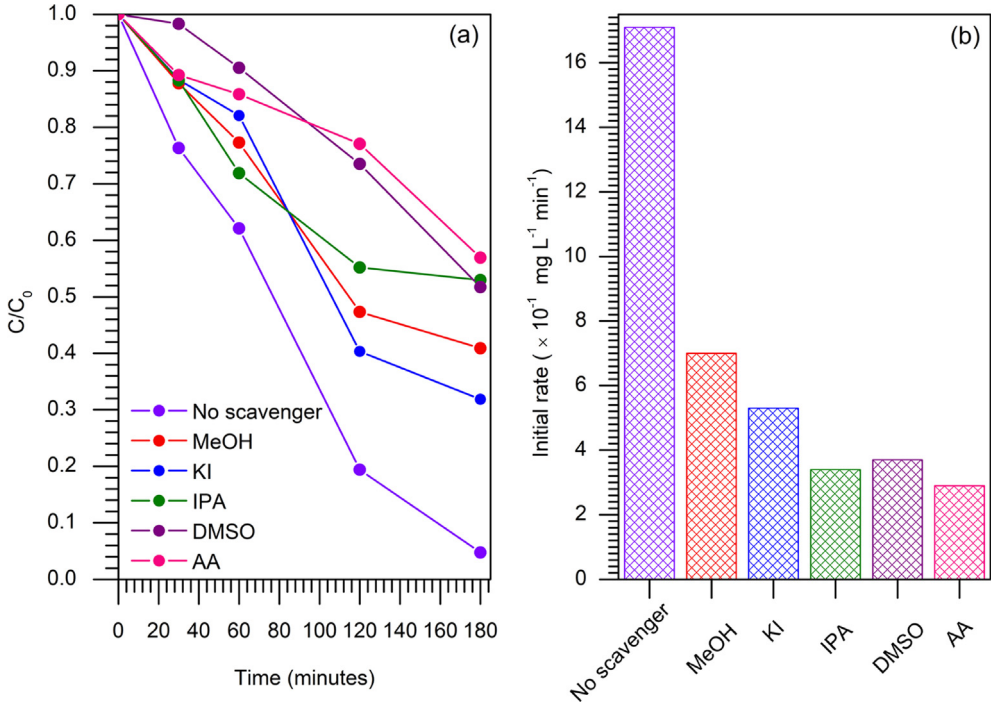

Fig. 16 Effect of scavenger molecules in photodegradation of methylene blue (C_{MB} = 100 mg L^{-1}, W = 1 g L^{-1}, t = 3 h, 33 ± 3 °C). (a) plot C/C0 versus time irradiation and (b) initial photodegradation rate in the presence of scavenger molecule.

showed the efficiency of MB degradation reduced to only 55%. When KI was added in the solution, the degradation was reduced to 65% suggesting MB degradation also catalysed by the hydroxyl radical produced on the surface of TiO_2/ZSM-5 (Fernandes et al., 2020). The investigation was further carried out by using IPA as scavenger of $\bullet OH_{bulk}$ (Aziz et al., 2021a), which indicated the reduction of efficiency to 45%. When DMSO as e^- scavenger (Allagui et al., 2019) was added, the degradation reduced to 46%, meanwhile AA further reduced the degradation to 42% suggesting the scavenging of $\bullet O_2^-$ (Omrani and Nezamzadeh-Ejhieh, 2020). In general, the presence of scavenger in the solution was detrimental towards the efficiency of MB photodegradation rate which implied that all species participated in the photocatalytic reaction. The slowest degradation rate was observed following the addition of ascorbic acid indicating the $\bullet O_2^-$ was the main active species in the photocatalytic reaction. Nevertheless, the apparent decrease in the rate constant of ascorbic acid were approximately similar with the addition of IPA and DMSO. These results also suggested that apart from $\bullet O_2^-$, $\bullet OH_{bulk}$, and e^- also played major roles as active species in degradation of MB.

4. Conclusion

TiO_2 deposited on mesoporous ZSM-5 via sol gel method improved the removal of MB, RhB and MG via adsorption and photodegradation. The studies explore the potential of RM as industrial waste from refining of bauxite, to be utilised as precursor for the synthesis of mesoporous ZSM-5. The as-synthesised ZSM-5 exhibited mesoporosity with diameter between 3.5 nm which was ideal for diffusion of MB molecules. Incorporation with TiO_2 further enhanced the removal of MB via adsorption-photodegradation pathways. However, controlling the amount of TiO_2 loading was crucial to ensure incorporation of TiO_2 did not annihilate the active sites for MB adsorption. The synergy between adsorption and photodegradation indicated the optimum adsorption–desorption equilibrium was crucial for efficient degradation of MB. Optimization studies on the effect of TiO_2 loading revealed 10% of TiO_2 on ZSM-5 exhibited a higher activity due to the increase of photosensitive sites while preserving most of the adsorption sites. The combination of high mesopore volume, large external surface area and TiO_2 loading were crucial to achieve the synergy between adsorption and photodegradation. $\bullet O_2^-$, $\bullet OH$, and e^- were identified as the major active species for MB photodegradation due to the reduction of photodegradation rate following introduction of scavenger molecules. TiO_2/ZSM-5 showed a good performance and reusability after 4 reaction cycles, with its potential can be extended for degradation of MG and RhB.

CRediT authorship contribution statement

Riki Subagyo: . **Hellna Tehubijuluw:** . **Wahyu Prasetyo Utomo:** . **Hamdan Dwi Rizqi:** . **Yuly Kusumawati:** Writing – review & editing. **Hasliza Bahruji:** Supervision. **Didik Prasetyoko:** Supervision, Funding acquisition.

Declaration of Competing Interest

The authors declare that they have no known competing financial interests or personal relationships that could have appeared to influence the work reported in this paper.

Acknowledgements

The author gratefully acknowledges The Deputy for Research and Development, Ministry of Research and Technology of Republic Indonesia for the research funding PDUPT scheme No 937/PKS/ITS/2021. The author also acknowledges Dr. Yun Hau NG from Catalysis for Alternative and Renewable energy (CARE) Laboratory, City University of Hong Kong and his team for their help with optical characterization.

Appendix A. Supplementary data

Supplementary data to this article can be found online at https://doi.org/10.1016/j.arabjc.2022.103754.

References

Al-Jubouri, S.M., 2020. Synthesis of hierarchically porous ZSM-5 zeolite by self-assembly induced by aging in the absence of seeding-assistance. Micropor. Mesopor. Mater. 303, 110296. https://doi.org/10.1016/j.micromeso.2020.110296.

Allagui, L., Chouchene, B., Gries, T., Medjahdi, G., Girot, E., Framboisier, X., Amara, A.B. haj, Balan, L., Schneider, R., 2019. Core/shell rGO/BiOBr particles with visible photocatalytic activity towards water pollutants. Appl. Surf. Sci. 490, 580–591. https://doi.org/10.1016/j.apsusc.2019.06.091.

Azami, M.S., Jalil, A.A., Hassan, N.S., Hussain, I., Fauzi, A.A., Aziz, M.A.A., 2021. Green carbonaceous material-fibrous silica-titania composite photocatalysts for enhanced degradation of toxic 2-chlorophenol. J. Hazard. Mater. 414, 125524. https://doi.org/10.1016/j.jhazmat.2021.125524.

Aziz, F.F.A., Jalil, A.A., Hassan, N.S., Fauzi, A.A., Azami, M.S., 2021a. Simultaneous photocatalytic reduction of hexavalent chromium and oxidation of p-cresol over AgO decorated on fibrous silica zirconia. Environ. Pollut. 285, 117490. https://doi.org/10.1016/j.envpol.2021.117490.

Aziz, F.F.A., Jalil, A.A., Hassan, N.S., Hitam, C.N.C., Rahman, A.F.A., Fauzi, A.A., 2021b. Enhanced visible-light driven multi-photoredox Cr(VI) and p-cresol by Si and Zr interplay in fibrous silica-zirconia. J. Hazard. Mater. 401, 123277. https://doi.org/10.1016/j.jhazmat.2020.123277.

Aziz, F.F.A., Jalil, A.A., Triwahyono, S., Mohamed, M., 2018. Controllable structure of fibrous SiO 2 –ZSM-5 support decorated with TiO 2 catalysts for enhanced photodegradation of paracetamol. Appl. Surf. Sci. 455, 84–95. https://doi.org/10.1016/j.apsusc.2018.05.183.

Bedin, K.C., Martins, A.C., Cazetta, A.L., Pezoti, O., Almeida, V.C., 2016. KOH-activated carbon prepared from sucrose spherical carbon: Adsorption equilibrium, kinetic and thermodynamic studies for Methylene Blue removal. Chem. Eng. J. 286, 476–484. https://doi.org/10.1016/j.cej.2015.10.099.

Belviso, C., Kharchenko, A., Agostinelli, E., Cavalcante, F., Peddis, D., Varvaro, G., Yaacoub, N., Mintova, S., 2018. Red mud as aluminium source for the synthesis of magnetic zeolite. Micropor. Mesopor. Mater. 270, 24–29. https://doi.org/10.1016/j.micromeso.2018.04.038.

Brião, G.V., Jahn, S.L., Foletto, E.L., Dotto, G.L., 2017. Adsorption of crystal violet dye onto a mesoporous ZSM-5 zeolite synthetized using chitin as template. J. Colloid Interface Sci. 508, 313–322. https://doi.org/10.1016/j.jcis.2017.08.070.

Cheng, Y., Xu, L., Jiang, Z., Liu, C., Zhang, Q., Zou, Y., Chen, Y., Li, J., Liu, X., 2021. Feasible low-cost conversion of red mud into magnetically separated and recycled hybrid SrFe12O19@NaP1 zeolite as a novel wastewater adsorbent. Chem. Eng. J. 417, 128090. https://doi.org/10.1016/j.cej.2020.128090.

Cui, H., Liang, Z., Zhang, J., Liu, H., Shi, J., 2016. Enhancement of the photocatalytic activity of a TiO2/carbon aerogel based on a hydrophilic secondary pore structure. RSC Adv. 6, 68416–68423. https://doi.org/10.1039/c6ra08074j.

Dao, T.B.T., Ha, T.T.L., Nguyen, T.D., Le, H.N., Ha-Thuc, C.N., Nguyen, T.M.L., Perre, P., Nguyen, D.M., 2021. Effectiveness of photocatalysis of MMT-supported TiO2 and TiO2 nanotubes for rhodamine B degradation. Chemosphere 280. https://doi.org/10.1016/j.chemosphere.2021.130802.

Derakhshan-Nejad, A., Rangkooy, H.A., Cheraghi, M., Yengejeh, R. J., 2020. Removal of ethyl benzene vapor pollutant from the air using TiO2 nanoparticles immobilized on the ZSM-5 zeolite under UVradiation in lab scale. J. Environ. Heal. Sci. Eng. 18, 201–209. https://doi.org/10.1007/s40201-020-00453-4.

Deshmukh, S.P., Kale, D.P., Kar, S., Shirsath, S.R., Bhanvase, B.A., Saharan, V.K., Sonawane, S.H., 2020. Ultrasound assisted preparation of rGO/TiO2 nanocomposite for effective photocatalytic degradation of methylene blue under sunlight. Nano-Structures & Nano-Objects 21, 100407. https://doi.org/10.1016/J.NANOSO.2019.100407.

Fauzi, A.A., Jalil, A.A., Hassan, N.S., Aziz, F.F.A., Azami, M.S., Hussain, I., Saravanan, R., Vo, D.V.N., 2022. A critical review on relationship of CeO2-based photocatalyst towards mechanistic degradation of organic pollutant. Chemosphere 286. https://doi.org/10.1016/j.chemosphere.2021.131651.

Fernandes, E., Martins, R.C., Gomes, J., 2020. Photocatalytic ozonation of parabens mixture using 10% N-TiO2 and the effect of water matrix. Sci. Total Environ. 718, 137321. https://doi.org/10.1016/j.scitotenv.2020.137321.

Frunza, L., Diamandescu, L., Zgura, I., Frunza, S., Ganea, C.P., Negrila, C.C., Enculescu, M., Birzu, M., 2018. Photocatalytic activity of wool fabrics deposited at low temperature with ZnO or TiO2 nanoparticles: Methylene blue degradation as a test reaction. Catal. Today 306, 251–259. https://doi.org/10.1016/j.cattod.2017.02.044.

Gomes, H.I., Mayes, W.M., Rogerson, M., Stewart, D.I., Burked, I.T., 2016. Alkaline residues and the environment: A review of impacts, management practices and opportunities. J. Clean. Prod. 112, 3571–3582. https://doi.org/10.1016/j.jclepro.2015.09.111.

Guo, N., Zeng, Y., Li, H., Xu, X., Yu, H., Han, X., 2018. Novel mesoporous TiO2@g-C3N4 hollow core@shell heterojunction with enhanced photocatalytic activity for water treatment and H2 production under simulated sunlight. J. Hazard. Mater. 353, 80–88. https://doi.org/10.1016/j.jhazmat.2018.03.044.

Hafeez, H.Y., Lakhera, S.K., Narayanan, N., Harish, S., Hayakawa, Y., Lee, B.K., Neppolian, B., 2019. Environmentally Sustainable Synthesis of a CoFe2O4-TiO2/rGO Ternary Photocatalyst: A Highly Efficient and Stable Photocatalyst for High Production of Hydrogen (Solar Fuel). ACS Omega 4, 880–891. https://doi.org/10.1021/acsomega.8b03221.

Han, X., An, L., Hu, Y., Li, Y., Hou, C., Wang, H., Zhang, Q., 2020. Ti3C2 MXene-derived carbon-doped TiO2 coupled with g-C3N4 as the visible-light photocatalysts for photocatalytic H2 generation. Appl. Catal. B Environ. 265, 118539. https://doi.org/10.1016/j.apcatb.2019.118539.

Hartati, Trisunaryanti, W., Mukti, R.R., Kartika, I.A., Firda, P.B.D., Sumbogo, S.D., Prasetyoko, D., Bahruji, H., 2020. Highly selective hierarchical ZSM-5 from kaolin for catalytic cracking of Calophyllum inophyllum oil to biofuel. J. Energy Inst. 93, 2238–2246. https://doi.org/10.1016/J.JOEI.2020.06.006.

He, J., Chen, D., Li, N., Xu, Q., Li, H., He, J., Lu, J., 2020. Controlled fabrication of mesoporous ZSM-5 zeolite-supported PdCu alloy nanoparticles for complete oxidation of toluene. Appl. Catal. B Environ. 265, 118560. https://doi.org/10.1016/j.apcatb.2019.118560.

Huang, T., Yan, M., He, K., Huang, Z., Zeng, G., Chen, A., Peng, M., Li, H., Yuan, L., Chen, G., 2019. Efficient removal of methylene blue from aqueous solutions using magnetic graphene oxide modified zeolite. J. Colloid Interface Sci. 543, 43–51. https://doi.org/10.1016/j.jcis.2019.02.030.

Joseph, A., Vellayan, K., González, B., Vicente, M.A., Gil, A., 2019. Effective degradation of methylene blue in aqueous solution using Pd-supported Cu-doped Ti-pillared montmorillonite catalyst. Appl. Clay Sci. 168, 7–10. https://doi.org/10.1016/j.clay.2018.10.009.

Khan, M.M., Ansari, S.A., Pradhan, D., Ansari, M.O., Han, D.H., Lee, J., Cho, M.H., 2014. Band gap engineered TiO2 nanoparticles for visible light induced photoelectrochemical and photocatalytic studies. J. Mater. Chem. A 2, 637–644. https://doi.org/10.1039/c3ta14052k.

Kusumawati, Y., Pauporté, T., Viana, B., Zouzelka, R., Remzova, M., Rathousky, J., 2017. Mesoporous TiO 2 /graphene composite films for the photocatalytic degradation of eco-persistent pollutants, in: Oxide-Based Materials and Devices VIII. Proc. SPIE, United States, p. 1010529. https://doi.org/10.1117/12.2253132.

Li, S., Ng, Y.H., Zhu, R., Lv, S., Wu, C., Liu, Y., Jing, L., Deng, J., Dai, H., 2021. In situ construction of elemental phosphorus nanorod-modified TiO2 photocatalysts for efficient visible-light-driven H2 generation. Appl. Catal. B Environ. 297, 120412. https://doi.org/10.1016/j.apcatb.2021.120412.

Li, Z., Wang, G., Zhai, K., He, C., Li, Q., Guo, P., 2018. Methylene blue adsorption from aqueous solution by loofah sponge-based porous carbons. Colloids Surfaces A Physicochem. Eng. Asp. 538, 28–35. https://doi.org/10.1016/j.colsurfa.2017.10.046.

Lin, Z., Du, C., Yan, B., Wang, C., Yang, G., 2018. Two-dimensional amorphous NiO as a plasmonic photocatalyst for solar H2 evolution. Nat. Commun. 9, 1–11. https://doi.org/10.1038/s41467-018-06456-y.

Liu, T., Wang, H., Hu, Z., Wei, F., 2021. Highly efficient adsorption of thiol compounds by ZSM-5 zeolites: Governing mechanisms. Micropor. Mesopor. Mater. 316, 110968. https://doi.org/10.1016/j.micromeso.2021.110968.

Ma, J., Huang, D., Zhang, W., Zou, J., Kong, Y., Zhu, J., Komarneni, S., 2016. Nanocomposite of exfoliated bentonite/g-C3N4/Ag3PO4 for enhanced visible-light photocatalytic decomposition of Rhodamine B. Chemosphere 162, 269–276. https://doi.org/10.1016/j.chemosphere.2016.07.089.

Ma, L., Wang, G., Jiang, C., Bao, H., Xu, Q., 2018. Synthesis of core-shell TiO 2 @g-C 3 N 4 hollow microspheres for efficient photocatalytic degradation of rhodamine B under visible light. Appl. Surf. Sci. 430, 263–272. https://doi.org/10.1016/j.apsusc.2017.07.282.

Makuła, P., Pacia, M., Macyk, W., 2018. How To Correctly Determine the Band Gap Energy of Modified Semiconductor Photocatalysts Based on UV-Vis Spectra. J. Phys. Chem. Lett. 9, 6814–6817. https://doi.org/10.1021/acs.jpclett.8b02892.

Mekprasart, W., Pavasupree, S., Jayasankar, C.K., Ravuri, B.R., Wattanawikkam, C., Pecharapa, W., 2021. Characterization, X-ray Absorption Spectroscopic Analysis and Photocatalytic Activity of Co/Zn Co-Doped TiO2 Nanoparticles Synthesized by One-Step Sonochemical Process. Crystals 11, 1254. https://doi.org/10.3390/CRYST11101254.

Mustapha, F.H., Jalil, A.A., Mohamed, M., Triwahyono, S., Hassan, N.S., Khusnun, N.F., Hitam, C.N.C., Rahman, A.F.A., Firmanshah, L., Zolkifli, A.S., 2017. New insight into self-modified surfaces with defect-rich rutile TiO2 as a visible-light-driven photocatalyst. J. Clean. Prod. 168, 1150–1162. https://doi.org/10.1016/j.jclepro.2017.09.095.

Na, J., Liu, G., Zhou, T., Ding, G., Hu, S., Wang, L., 2013. Synthesis and catalytic performance of ZSM-5/MCM-41 zeolites with varying mesopore size by surfactant-directed recrystallization. Catal. Letters 143, 267–275. https://doi.org/10.1007/s10562-013-0963-0.

Omrani, N., Nezamzadeh-Ejhieh, A., 2020. A ternary Cu2O/BiVO4/WO3 nano-composite: Scavenging agents and the mechanism pathways in the photodegradation of sulfasalazine. J. Mol. Liq. 315, 113701. https://doi.org/10.1016/j.molliq.2020.113701.

Pan, Y., Zhang, Y., Huang, Y., Jia, Y., Chen, L., Cui, H., 2021. Synergistic effect of adsorptive photocatalytic oxidation and degradation mechanism of cyanides and Cu/Zn complexes over TiO2/ZSM-5 in real wastewater. J. Hazard. Mater. 416, 125802. https://doi.org/10.1016/j.jhazmat.2021.125802.

Park, J.A., Yang, B., Lee, J., Kim, I.G., Kim, J.H., Choi, J.W., Park, H.D., Nah, I.W., Lee, S.H., 2018. Ultrasonic spray pyrolysis synthesis of reduced graphene oxide/anatase TiO2 composite and its application in the photocatalytic degradation of methylene blue in water. Chemosphere 191, 738–746. https://doi.org/10.1016/j.chemosphere.2017.10.094.

Pathania, D., Sharma, S., Singh, P., 2017. Removal of methylene blue by adsorption onto activated carbon developed from Ficus carica bast. Arab. J. Chem. 10, S1445–S1451. https://doi.org/10.1016/j.arabjc.2013.04.021.

Peñas-Garzón, M., Gómez-Avilés, A., Belver, C., Rodriguez, J.J., Bedia, J., 2020. Degradation pathways of emerging contaminants using TiO2-activated carbon heterostructures in aqueous solution under simulated solar light. Chem. Eng. J. 392, 124867. https://doi.org/10.1016/j.cej.2020.124867.

Qin, Y., Wang, L., Zhao, C., Chen, D., Ma, Y., Yang, W., 2016. Ammonium-Functionalized Hollow Polymer Particles As a pH-Responsive Adsorbent for Selective Removal of Acid Dye. ACS Appl. Mater. Interfaces 8, 16690–16698. https://doi.org/10.1021/ACSAMI.6B04199.

Rahman, A.F.A., Jalil, A.A., Triwahyono, S., Ripin, A., Aziz, F.F.A., Fatah, N.A.A., Jaafar, N.F., Hitam, C.N.C., Salleh, N.F.M., Hassan, N.S., 2017. Strategies for introducing titania onto mesostructured silica nanoparticles targeting enhanced photocatalytic activity of visible-light-responsive Ti-MSN catalysts. J. Clean. Prod. 143, 948–959. https://doi.org/10.1016/j.jclepro.2016.12.026.

Santoso, E., Ediati, R., Kusumawati, Y., Bahruji, H., Sulistiono, D.O., Prasetyoko, D., 2020. Review on recent advances of carbon based adsorbent for methylene blue removal from waste water. Mater. Today Chem. 16, 100233. https://doi.org/10.1016/J.MTCHEM.2019.100233.

Shams-Ghahfarokhi, Z., Nezamzadeh-Ejhieh, A., 2015. As-synthesized ZSM-5 zeolite as a suitable support for increasing the photoactivity of semiconductors in a typical photodegradation process. Mater. Sci. Semicond. Process. 39, 265–275. https://doi.org/10.1016/j.mssp.2015.05.022.

Shi, J.W., Cui, H.J., Chen, J.W., Fu, M.L., Xu, B., Luo, H.Y., Ye, Z. L., 2012. TiO 2/activated carbon fibers photocatalyst: Effects of coating procedures on the microstructure, adhesion property, and photocatalytic ability. J. Colloid Interface Sci. 388, 201–208. https://doi.org/10.1016/j.jcis.2012.08.038.

Svyatchenko, V.A., Nikonov, S.D., Mayorov, A.P., Gelfond, M.L., Loktev, V.B., 2021. Antiviral photodynamic therapy: Inactivation and inhibition of SARS-CoV-2 in vitro using methylene blue and Radachlorin. Photodiagnosis Photodyn. Ther. 33, 102112. https://doi.org/10.1016/j.pdpdt.2020.102112.

Tang, S., Xia, D., Yao, Y., Chen, T., Sun, J., Yin, Y., Shen, W., Peng, Y., 2019. Dye adsorption by self-recoverable, adjustable amphiphilic graphene aerogel. J. Colloid Interface Sci. 554, 682–691. https://doi.org/10.1016/j.jcis.2019.07.041.

Tang, X., Feng, Q., Liu, K., Luo, X., Huang, J., Li, Z., 2018. A simple and innovative route to remarkably enhance the photocatalytic performance of TiO2: Using micro-meso porous silica nanofibers as carrier to support highly-dispersed TiO2 nanoparticles. Micropor. Mesopor. Mater. 258, 251–261. https://doi.org/10.1016/j.micromeso.2017.09.024.

Tehubijuluw, H., Subagyo, R., Yulita, M.F., Nugraha, R.E., Kusumawati, Y., Bahruji, H., Jalil, A.A., Hartati, H., Prasetyoko, D., 2021. Utilization of red mud waste into mesoporous ZSM-5 for methylene blue adsorption-desorption studies. Environ. Sci. Pollut. Res. 28, 37354–37370. https://doi.org/10.1007/s11356-021-13285-y.

Tkaczyk, A., Mitrowska, K., Posyniak, A., 2020. Synthetic organic dyes as contaminants of the aquatic environment and their implications for ecosystems: A review. Sci. Total Environ. 717, 137222. https://doi.org/10.1016/j.scitotenv.2020.137222.

Wang, M., Liu, X., 2021. Applications of red mud as an environmental remediation material: A review. J. Hazard. Mater. 408,. https://doi.org/10.1016/j.jhazmat.2020.124420 124420.

Wang, Y., Cheng, Y. Shen, Yu, M. Gao, Li, Y., Cao, J. Liang, Zheng, L. Gang, Yi, H. Wei, 2017. Methane explosion suppression characteristics based on the NaHCO3/red-mud composite powders with core-shell structure. J. Hazard. Mater. 335, 84–91. https://doi.org/10.1016/j.jhazmat.2017.04.031.

Weber, J., Thompson, A., Wilmoth, J., Batra, V.S., Janulaitis, N., Kastner, J.R., 2019. Effect of metal oxide redox state in red mud catalysts on ketonization of fast pyrolysis oil derived oxygenates. Appl. Catal. B Environ. 241, 430–441. https://doi.org/10.1016/j.apcatb.2018.08.061.

Wellia, D.V., Kusumawati, Y., Diguna, L.J., Pratiwi, N., Putri, R.A., Amal, M.I., 2020. Mesoporous Materials for Degradation of Textile Dyes. In: Naushad, M., Srivastava, R., Lichtfouse, E. (Eds.), Green Methods for Wastewater Treatment. Springer, Cham, Switzerland, pp. 255–288. https://doi.org/10.1007/978-3-030-16427-0_10.

Yang, W., Hussain, A., Zhang, J., Liu, Y., 2018. Removal of elemental mercury from flue gas using red mud impregnated by KBr and KI reagent. Chem. Eng. J. 341, 483–494. https://doi.org/10.1016/j.cej.2018.02.023.

Ye, S., Zhou, X., Xu, Y., Lai, W., Yan, K., Huang, L., Ling, J., Zheng, L., 2019. Photocatalytic performance of multi-walled carbon nanotube/BiVO4 synthesized by electro-spinning process and its degradation mechanisms on oxytetracycline. Chem. Eng. J. 373, 880–890. https://doi.org/10.1016/j.cej.2019.05.109.

Znad, H., Abbas, K., Hena, S., Awual, M.R., 2018. Synthesis a novel multilamellar mesoporous TiO2/ZSM-5 for photo-catalytic degradation of methyl orange dye in aqueous media. J. Environ. Chem. Eng. 6, 218–227. https://doi.org/10.1016/j.jece.2017.11.077.

Zouzelka, R., Kusumawati, Y., Remzova, M., Rathousky, J., Pauporté, T., 2016. Photocatalytic activity of porous multiwalled carbon nanotube-TiO2 composite layers for pollutant degradation. J. Hazard. Mater. 317, 52–59. https://doi.org/10.1016/j.jhazmat.2016.05.056.